Advanced Functional Materials / Volume 33, Issue 33 / 2302866

Research Article | Full Access

Selective Surface Engineering of Perovskite Microwire Arrays

Dengji Li, You Meng, Yuxuan Zhang, Pengshan Xie, Zixin Zeng, Wei Wang, Zhengxun Lai, Weijun Wang, Sai-Wing Tsang, Fei Wang, Chuntai Liu, Changyong Lan, SenPo Yip, Johnny C. Ho

First published: 01 May 2023
https://doi-org.fgul.idm.oclc.org/10.1002/adfm.202302866
Citations: 3

Abstract

The surface of low-dimensional perovskites play a crucial role in determining their intrinsic property. Understanding their characteristics and the influence of certain surfaces is valuable in designing functional surface-engineered structures. Meanwhile, surface passivation can also be applied to stabilize and optimize the state-of-the-art perovskite-based optoelectronics. Herein, cesium lead bromide ($CsPbBr_3$) microwire parallel arrays are designed and fabricated with specific (100)-terminated crystal planes, which exhibit excellent photodetection performance with long-term environment stability >3000 h. Notably, it is uncovered experimentally and theoretically that environmental oxygen can not only passivate the Br-vacancy-related trap states on the (100) surface, but also create charge carrier nanochannels to enhance the (opto)electronic properties. The coupling effects between oxygen species and the specific terminated crystal planes of perovskites highlight the importance of surface engineering for designing and optimizing perovskite-based devices.

1 Introduction

The surface of materials is the exposed terminated crystal plane, which dominates the physical/chemical properties of micro- or nanoscale materials.[1] Specific preferred surface engineering on certain crystal planes could be considered the advanced process to understand and manipulate the surface science,[2] and significantly affect the optoelectronic performance of semiconductor devices.[3] Compared to the bulk crystal, the all-inorganic halide perovskites (HPs) micro/nanowires have been demonstrated with excellent

optoelectronic properties attributable to their unique 1D structure and potential contributions of surface engineering.[4] It is noted that the (100) planes of HPs crystals have been experimentally proven to exhibit higher carrier mobility and longer carrier lifetime than those of other terminated surfaces.[5] Meanwhile, based on the theoretical simulation (Figure S1, Supporting Information), the (100) surface of the HPs structure, for example, cesium lead bromide ($CsPbBr_3$), indeed possesses the lowest surface bandgap energy (1.92 eV) among all the surfaces, inherently broadening the light-harvesting wavelength range.

On the other hand, surface passivation has also been developed to enhance the optoelectronic performance and long-term stability of perovskites.[6] Especially, environmental gases are well known to have a considerable regulatory effect on the optoelectronic properties of HPs surfaces.[7] For instance, the surface passivation of HPs with oxygen gas has been proposed to enhance light-emission efficiencies and spontaneous carrier recombination lifetimes, owing to the passivation to traps induced by halide vacancies.[8] However, the surface engineering and surface passivation on the specific surface of HPs and the corresponding differentiation effect are still missing. An in-depth understanding of the interaction between specific HPs surfaces and surrounding environmental gases is essential for the further performance enhancement of HP devices.

Herein, we successfully designed and realized the high-quality $CsPbBr_3$ microwire (MW) parallel arrays with specifically terminated (100) surfaces. Based on these selective (100) microwire surfaces, the fabricated photodetectors (PDs) exhibit excellent optoelectronic performance with a high on/off ratio of 5×10^4, a large responsivity of 263 A W^{-1}, an impressive detectivity of 1.06×10^{12} Jones, fast rise and recovery times of 94 and 136 µs. More importantly, these (100) surface-terminated $CsPbBr_3$ MW parallel arrayed PDs unveil outstanding long-term ambient stability >3000 h. It is verified that oxygen passivation enhances the performance of PDs, which is supported by a series of surface characterization analyses. Through density functional theory (DFT) calculations, we reveal that trap states caused by surface bromine vacancy (Br-vacancy) can be eliminated with oxygen passivation and thus significantly reduce the nonradiative recombination, leading to better optoelectronic performance. Besides, the occupied oxygen species can also form a fast transfer nanochannel for the charge carriers, thus enhancing the photocurrent. Our results highlight the selective surface engineering strategy for achieving improved device performance and long-term stability on HPs.

2 Results and Discussion

To date, several strategies have been explored to obtain 1D HPs structures with desired morphology, such as capillary-bridge-manipulated graphoepitaxy[9] and substrate surface energy-mediated growth.[10] Most recently, by using a capillary-bridge assembly method, gradient bandgap-tunable single-crystalline perovskite MWs arrays with pure

crystallographic orientation were produced to show improved color recognition performances.[11] Different from the above methods, the surface-guided van der Waals epitaxial effect is utilized to obtain the horizontal alignment of HPs MWs in this work.[12] Distinct from previous related works,[13] which mainly explored the formation process and characterization of materials, our study aims to investigate the role of crystal planes in determining the optoelectronic properties of the $CsPbBr_3$ perovskite. Here, using the chemical vapor deposition (CVD) process, high-quality single-crystalline $CsPbBr_3$ MW parallel arrays are successfully synthesized on muscovite mica substrates (more experimental details in the Experimental Section). At the same time, the schematic illustration of the growth system is displayed in Figure S2 (Supporting Information). Meanwhile, the precise manipulation of $CsPbBr_3$ MW size and morphology is achieved by optimizing the growth time, temperature, substrate location, and other process parameters.

Figure 1a,b illustrate the employed growth model of $CsPbBr_3$ MW arrays on mica substrates, in which triangular prism MWs are found to grow along the [001] direction with specific (100) exposed facets. The atomic arrangement with the (110) plane of $CsPbBr_3$ on the (001) plane of mica is displayed in Figure 1d (front view) and Figure S3 (Supporting Information) (top view), in which the epitaxial growth of $CsPbBr_3$ satisfies the orientation characteristics of $CsPbBr_3$[001] // mica[010] and $CsPbBr_3$[110] // mica[100].[4, 11] Also, as shown in the atomic force microscope (AFM) images in Figure 1c and Figure S4 (Supporting Information), the perovskite MW arrays exhibit the unique triangular prism structure with a mathematical relationship between the height (H) and the width (W) of as-grown $CsPbBr_3$ MW samples, i.e., H = 0.5 W. The scanning electron microscope (SEM) result further confirms that these triangular prism MWs have smooth and flat surfaces with perfect horizontal alignments lying on the substrates (Figure 1f,g).

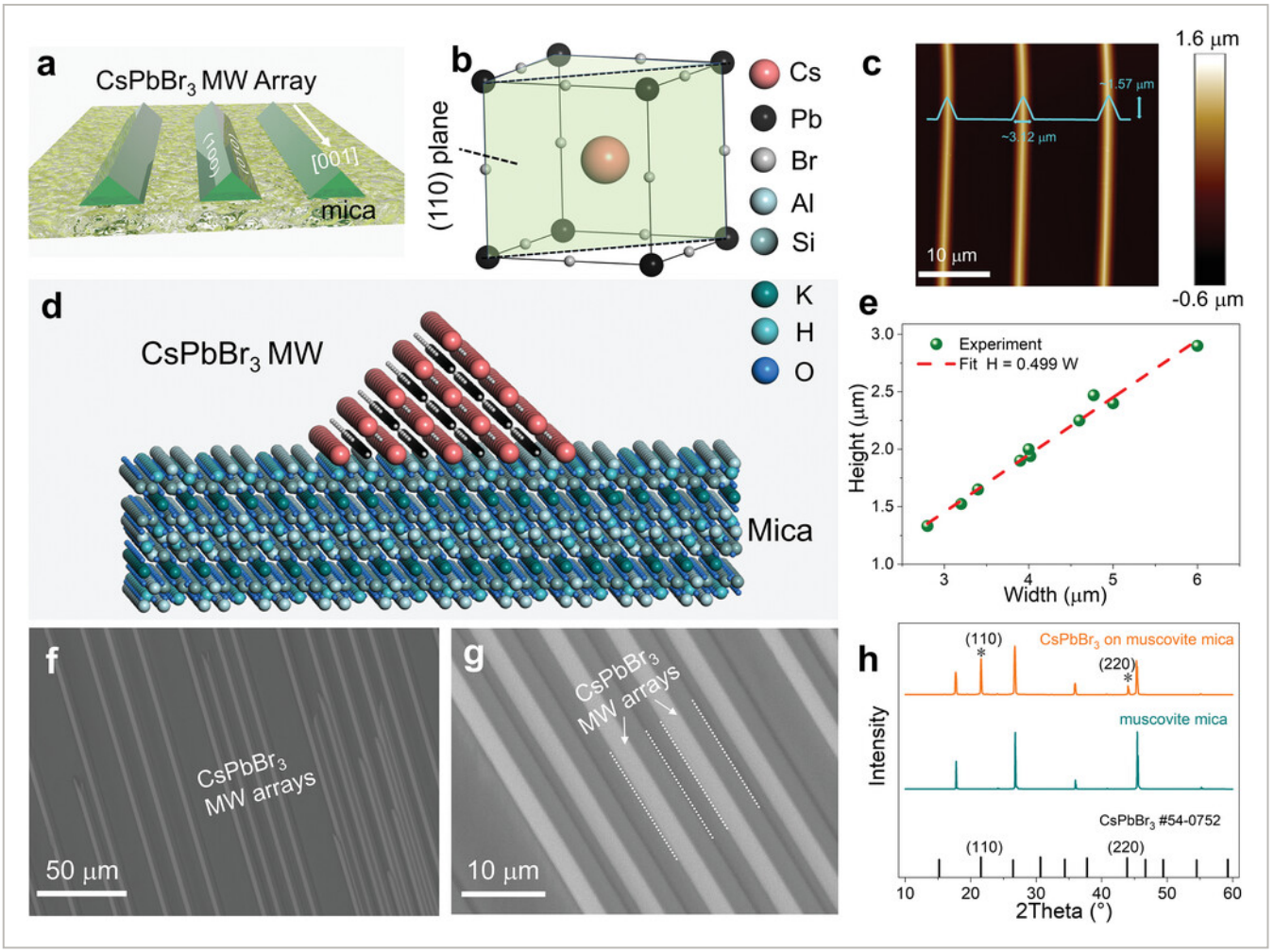

Figure 1

Open in figure viewer | PowerPoint

Growth model and characterizations of $CsPbBr_3$ MW parallel arrays. a) Schematic diagram of the $CsPbBr_3$ MW parallel arrays on mica. b) Illustration of the as-grown triangular prism microwire (coated with green color) in the cubic $CsPbBr_3$ unit cell structure, while the (110) plane is indicated by dotted lines. c) AFM image of as-grown $CsPbBr_3$ MW arrays. d) The front view of the atomic arrangement of $CsPbBr_3$ MW on mica. e) Statistical results about the morphology relationship of the fabricated perovskite MW, revealing the mathematic relationship of "Height = 0.5 Width". f, g) SEM images of the $CsPbBr_3$ MW arrays grown on mica. h) XRD pattern of the perovskite MW arrays grown on mica and the initial muscovite mica, together with the standard XRD for cubic $CsPbBr_3$ (#54-0752).

Next, the energy-dispersive X-ray spectroscopy (EDS) mapping was carried out to analyze the elemental distribution (Figure S5, Supporting Information), from which Cs and Pb are uniformly distributed along the MW body. Meanwhile, O, K, and Si are also evenly distributed in the whole scope except the MW array, which is the characteristic signal of mica. Notably, the energy of Al $K\alpha_1$ is very close to that of Br $L\alpha_{1,2}$, where the signals are hard to be distinguished. The corresponding EDS spectrum indicates that the composition ratio of Cs, Pb, and Br is close to 1:1:3 (Figure S6, Supporting Information), agreeing with the stoichiometric ratio of $CsPbBr_3$. In addition, the PL pattern of the as-grown sample was also

investigated, in which the peak at the wavelength of 520 nm (Figure S7, Supporting Information) agrees well with the cubic-phase $CsPbBr_3$ characteristic peak.

The highly crystalline nature of the as-grown perovskite MW arrays was further verified by X-ray diffraction (XRD) patterns (Figure 1h), and the diffraction peaks at 21.6° and 43.05° agree well with the (110) and (220) planes of cubic-phase $CsPbBr_3$ (JCPDS #54-0752, , a = 5.83 Å). The absence of extra diffraction peaks from $CsPbBr_3$ strongly implies the van der Waals epitaxial growth with the (110) lattice planes parallel to the mica surface, directly confirming the growth model of perovskite MWs grown on mica. Therefore, all these characterization results demonstrate the specific (100) surface of cubic-phase $CsPbBr_3$ perovskite MW arrays with high crystallinity.

Once the perovskite MW arrays are fabricated, it is important to study their optoelectronic properties. The (100) surface-engineered structures of perovskite MW arrays were configured into a simple PD structure (Figure 2a). Specifically, after the perovskite MW arrays were grown on the mica substrate, 50 nm thick Au electrodes were thermally evaporated on the substrate through a shadow mask with a channel length of 15 µm. The SEM image of the PD structure was provided in the inset diagram of Figure 2b, while the corresponding current–voltage (I–V) curve was acquired in the dark and under different power intensities (0.1 to 30 mW cm^{-2}), as displayed in Figure 2b. When the 450 nm light is irradiated on the (100) surface, the photogenerated carriers are effectively separated and transported through the perovskite MWs.[14] Our experimental results demonstrate that the photocurrent increases with power intensity, indicating that more photogenerated carriers are created under the 450 nm source with increasing power intensity. This can be explained by the fact that increasing the power intensity leads to a greater number of photons interacting with the electrons, resulting in more electrons acquiring energy from the photons and transitioning from the valence band to the conduction band. It is worth mentioning that these (100) surface-based devices exhibit a dark current as low as 15 pA, whereas the output current enhances by 4.5 orders of magnitude to above 800 nA under 30 mW cm^{-2} illumination. The on-off switching characteristics (Figure 2c) demonstrate that the photocurrent tends to increase as the power intensity increases, which is consistent to the theory that the quantity of photogenerated carriers is proportional to the arriving photon flux.[15]

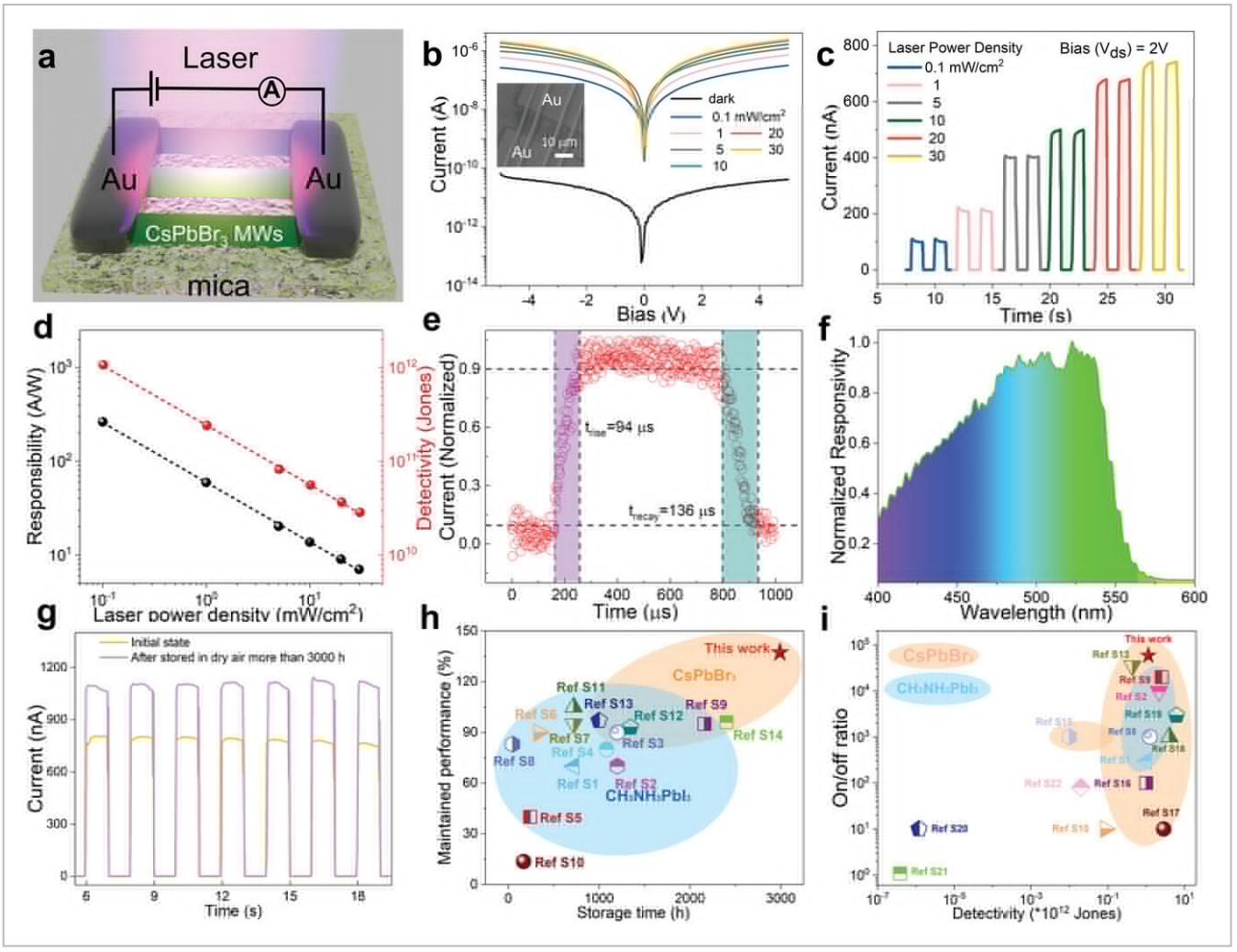

Figure 2

Open in figure viewer | PowerPoint

Characterizations of $CsPbBr_3$ MW arrays-based photodetectors. a) Schematic diagram of the photodetector device structure. b) Log *I*–*V* curves of the photodetector device. Inset is the SEM image of the device. c) *I*–*t* curve of the photodetector without and with 450 nm illumination of 0.1–30 mW cm^{-2} power density, while the source-drain bias is 2 V. d) Responsivity and detectivity versus power intensity of illumination. e) Response and recovery times of the device. f) Normalized spectral response of the device under the illumination of 400–600 nm wavelength. g) Time-resolved response of initial device and device stored >3000 h. h) Long-term stability and i) performance comparison with the state-of-the-art perovskite MWs or films. (Detailed comparison parameters are listed in Table S1, Supporting Information)

More importantly, to evaluate the performance of PD devices, there are two important figures of merit parameters, namely photoresponsivity (R) and detectivity (D^*), which can be directly extracted from the measurement results. The mathematical expression of R is described by the equation of $R = I_{ph}/PS$, where I_{ph} ($I_{ph} = I_{light} - I_{dark}$), P, and S are the photocurrent, incident power density illuminated on the MW array, and effective illumination area on the MW arrays, respectively. Meanwhile, another parameter, D^*, is

defined as $D^* = R(S\Delta f)^{1/2}/i_n$, where i_n is the noise current and Δf is the electrical bandwidth. Figure S8 (Supporting Information) exhibits that the noise current spectrum of $CsPbBr_3$ MW arrays PD is dominated by $1/f$ noise, with a bias voltage of 2 V. The noise of $CsPbBr_3$ MW arrays was measured as 0.539 pA/Hz$^{1/2}$ at 1 Hz. Consequently, we calculated the specific detectivity (D^*) of $CsPbBr_3$ MW arrays PD to be 1.06×10^{12} Jones (cm Hz$^{1/2}$ W^{-1}). Figure 2d displays the calculated R and D^* under different power densities, revealing both R and D^* tend to decrease with increasing power density. These decay trends in R and D^* were speculated to be caused by the trap states within the $CsPbBr_3$ MW body or at the surface of perovskite MWs.[16] At a relatively low light power intensity (0.1 mW cm^{-2}), the device reaches a high photoresponsivity of 263 A W^{-1} and a good detectivity of 1.06×10^{12} Jones, being comparable to the state-of-the-art perovskite-based photodetectors (Figure 2i). Furthermore, the device operation stability was also investigated, as provided in Figure S9 (Supporting Information). The device exhibits a relatively stable photo-switching performance in a continuous operation period of >65 h (Figure S9a,b, Supporting Information) under 5 mW cm^{-2} illumination, suggesting a potential prospect of our devices for practical applications.

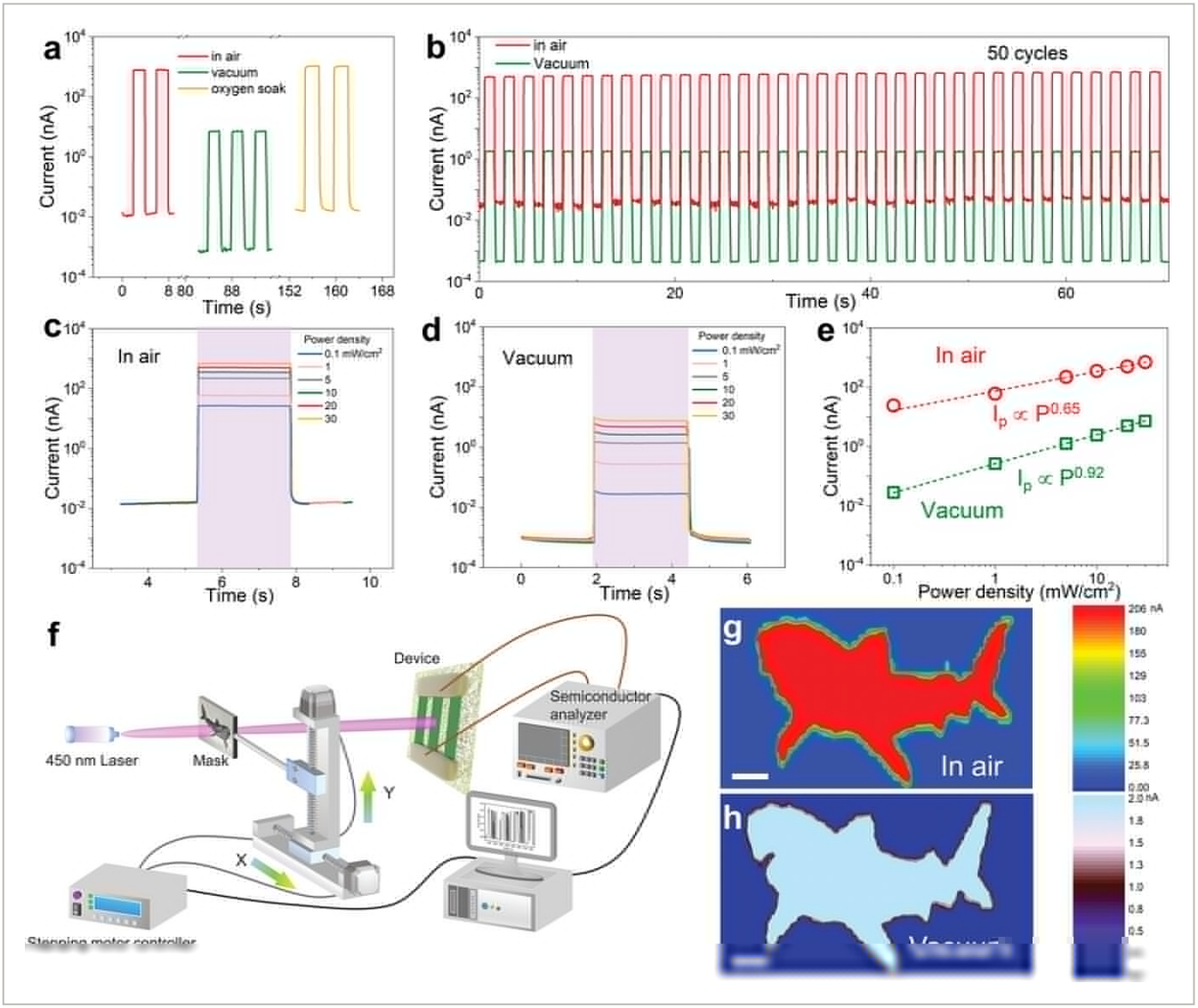

Figure 3

Characterizations of $CsPbBr_3$ MW arrays-based photodetectors in different conditions. a) Photo-switching curves recorded in air (red), vacuum (green), and pure oxygen (orange), while source-drain bias and power density are regulated as 2 V and 30 mW cm^{-2}, respectively. b) Photo-switching comparison curves in air (red) and under vacuum (green) for a constant measurement >50 loops. High-resolution time-resolved photo-switching curves c) in air and d) under vacuum. e) Current-power density curve acquired in air and under vacuum. f) Schematic diagram of the image sensing system. Converted "shark" image acquired g) in air and h) under vacuum. The scale bar is 20 pixels.

To acquire the precise response and recovery times of the devices, the on-off switching measurement was manipulated by a high-frequency chopper, while a digital oscilloscope recorded the temporal response. As displayed in Figure 2e, the response (purple) and recovery (blue) times, recognized as the time for the photocurrent to shift from 10% to 90% and from 90% to 10% of the maximum output signal, were found to be 94 and 136 µs, respectively. These results are faster than those of the previous photodetector devices based on perovskite nano/microwires arrays or films (Table S1, Supporting Information). To further investigate the spectral response, the device was continuously irradiated with wavelength changing from 400 to 600 nm. As presented in Figure 2f, the responsivity of the MW photodetector reaches a peak at ≈530 nm and then declines sharply at ≈560 nm, where this trend is consistent with the characteristic bandgap energy values calculated in Figure S1 (Supporting Information).[17]

At the same time, long-term stability is always regarded as a stumbling block for the practical and commercial development of perovskite-based photodetectors. Intriguingly, as illustrated in Figure 2g, the photocurrent of the perovskite MW arrays device gets enhanced to 140% of its initial value after being stored in ambient for 3000 h, demonstrating excellent resistance to the external environmental stimulus. The long-term stability of our devices is significantly improved, especially compared to the reported perovskite devices in Figure 2h. These impressive long-term stability and photocurrent enhancement can be mostly attributed to the impact of environmental oxygen on the perovskite MW (100) surfaces, which will be discussed later in details.

Subsequently, the comparison experiment was designed to assess the detection performance of the devices in air, vacuum, and pure oxygen environment, respectively. As shown in Figure 3a, the device exhibited a similar photocurrent under 30 mW cm^{-2} power density illumination in air and pure oxygen environment, but a remarkable photocurrent decline (about two orders) in the vacuum condition (≈10^{-4} Pa). To eliminate the influence of oxygen species, the vacuuming process was maintained for at least 36 h before measurement. Hence, we preliminarily consider oxygen as the main cause of enhancing the device's performance in the air. Based on the XRD patterns presented in Figure S10 (Supporting Information), both fresh and ambient-stored samples show similar diffraction

peaks, which excludes the possible influence of material decomposition on their optoelectronic properties.

Moreover, the short-term stability of devices in air and vacuum environment was also investigated. As shown in Figure 3b, the photo- and dark-current were measured under several photo-switching cycles, demonstrating again their operational stability. To further explore the physical nature of oxygen impact on the photodetection characteristics, the device was measured under different power densities (from 0.1 to 30 mW cm^{-2}) illumination both in air and under vacuum (Figure 3c,d), with the photocurrent for each condition extracted and compiled in Figure 3e. It is evident that all the experimental data is perfectly fitted by the power law equation of $I_{ph} \propto P^{\alpha}$. The extracted α values in air and under vacuum are calculated to be 0.65 and 0.92, respectively, which reveals the different optoelectronic properties of the (100) surface under those two conditions (i.e., air vs. vacuum).[18]

Besides, owing to the high sensitivity of $CsPbBr_3$ MWs in the visible light region, we demonstrated the applicability of our devices in the applications of image sensing. Figure 3f schematically illustrates the entire setup of the imaging system studied in this work. A 450 nm laser was adopted as the light source, while a patterned mask was hollowed-out to act as the image template. Hence, the laser beam could pass through the mask and illuminate the perovskite MW arrays PD. When the laser scanned the patterned mask (i.e., the shape of "shark"), a semiconductor analyzer could record the photoresponse in time-spatial revolution, converting it into the images of "shark" with high resolution under different environments (Figure 3g,h). Apparently, the "shark" recorded in air exhibits more distinct contrast than that acquired under vacuum, revealing an over two order-of-magnitude increase of photocurrent, directly demonstrating the sensitivity enhancement in oxygen-treated PD device.

After that, it is essential to gain deep insight into the physical origin of the oxygen passivation effect observed above. In this case, X-ray photoelectron spectroscopy (XPS) was performed to assess the interaction between the oxygen species and perovskite MW arrays. The corresponding XPS results under different environments are then displayed in Figure 4a. For the (100) surface terminated $CsPbBr_3$ MW arrays measured in the oxygen environment, the peaks at 137.3 and 142.3 eV are corresponded to Pb $4f_{7/2}$ and Pb $4f_{5/2}$, respectively. However, the broadened peak could be divided into two additional lower binding energy peaks at 136.9 and 141.9 eV, which could be assigned to the oxygen passivation effect.[8, 19] Accordingly, as the surrounding environment was pumped down to vacuum, the peaks of $4f_{7/2}$ and Pb $4f_{5/2}$ became narrower and sharper, whereas the peaks representing the oxygen passivation effect were close to vanishing. Hence, the XPS finding suggests the existence of oxygen on the (100) surface of all-inorganic $CsPbBr_3$ MW arrays in the ambient environment.

Figure 4

Characterization and theoretical calculations on the (100) surface of perovskites. a) XPS spectra of Pb $4f_{5/2}$ and $4f_{7/2}$ of the $CsPbBr_3$ MWs in oxygen and under vacuum. b) In situ PL spectra of the as-grown MW sample with pure oxygen injection. c) 2D contour image of the in situ PL spectra. d) PL decay dynamics of the sample in oxygen and under vacuum. Theoretical models of the $CsPbBr_3$ surface with e) Br-vacancy and f) oxygen-passivated vacancy. g) Calculated energy band structures of intrinsic, Br-vacancy, and oxygen-passivated surfaces. h) Calculated differential of charge density surrounding the passivated oxygen species.

More importantly, to further reveal the passivation effect of oxygen species on the carrier recombination pathways, an in situ PL spectroscopic study was carried out in a high vacuum condition, as well as in an oxygen environment. As displayed in Figure 4b, the PL intensity of the $CsPbBr_3$ characteristic peak at 520.6 nm enhances with time after introducing pure oxygen to the chamber. As the system was evacuated to vacuum, the peak intensity could recover to its initial state. Also, the visualization of the tracked PL spectrum during the transfer from vacuum to oxygen environments was displayed in Figure 4c, indicating the enhanced intensity of the maintained characteristic peak. This observation evidently suggests the passivation effect of oxygen species to the (100) surface of perovskite MW arrays. According to the previous work,[8] this PL intensity switching response caused by oxygen passivation is the characteristic effect of the surface Br-vacancy type perovskite, signifying the dominant Br-vacancy defects on the (100) surface of $CsPbBr_3$ MW arrays.

In addition, the double-exponential fitting curve was adopted to fit the time-resolved PL (TRPL) decay results in order to analyze the PL recombination dynamics of the perovskite MWs in different conditions (Figure 4d). In vacuum conditions, the extracted fast and slow components of PL lifetimes, τ_1 and τ_2, were determined to be 0.87 and 5.96 ns, respectively, which increased to 1.86 and 21.2 ns after oxygen injection. At the same time, the average lifetime, τ, can be estimated by the equation of $\tau = \Sigma_i A_i \tau_i^2 / \Sigma_i A_i \tau_i$, where A_i is the decay amplitude.[20] This way, the average lifetime, τ, was calculated to be 2.52 and 20.24 ns for vacuum and oxygen conditions, respectively. This increasing trend of PL lifetime caused by oxygen passivation indicates that the nonradiative recombination is suppressed owing to the reduced defect density passivated by oxygen species,[21] being consistent with the enhancing fluorescence intensity due to the oxygen species passivation to traps. Additionally, we have provided a detailed analysis of the SCLC results (Figure S11, Supporting Information) to evaluate the defect density. According to the literature,[22] the trap density (n_t) can be determined by trap-filled limit voltage (V_{TFL}),

(1)

where e is the electron charge, L is the channel length, ε (19.2) is relative dielectric constant of $CsPbBr_3$, and ε_0 is the vacuum permittivity. Hence, the trap density, n_t, of $CsPbBr_3$ in air was calculated to be 1.05×10^{14} cm^{-3}, which is lower than that in vacuum (4.68×10^{14} cm^{-3}),

indicating a fewer trap density in air condition. Our results demonstrate the effectiveness of our oxygen passivation strategy in reducing the trap density and improving the optoelectronic performance of the (100) surface of perovskite MW arrays.

Apart from evaluating the experimental results, first-principal density functional theory (DFT) simulations were conducted to thoroughly understand the passivation mechanism of these oxygen species on perovskites. The (100) surfaces of cubic $CsPbBr_3$ with Br vacancies and vacancies passivated by oxygen species are modeled in Figure 4e,f, respectively. Simultaneously, the perfect $CsPbBr_3$ surface model was also built and exhibited in Figure S12 (Supporting Information) for reference. To investigate the specific passivation effect of oxygen species passivation to the Br-vacancy, the band structures of these three models were calculated, and the corresponding results were displayed in Figure 4g. For the Br-vacancy surface, several distinct additional energy levels mainly originated from the *p*-orbital of Pb were beneath the conduction band (CB) edge, which was considered the trap states. These detrimental trap states would act as the center of nonradiative recombination, leading to the capture of photogenerated carriers and a shorter diffusion length, hence deteriorating the optoelectronic performance of the device.[23]

Consequently, with those vacancies occupied by oxygen species, these detrimental trap levels vanished in the energy band, while the entire energy band structure was similar to the intrinsic $CsPbBr_3$. The corresponding partial density of state (PDOS) results were also provided in Figure S13 (Supporting Information), illustrating more details of the calculated energy band structures. Besides, the differential charge density of the oxygen-passivated (100) surface to the Br-vacancy surface was calculated, and the corresponding result was presented in Figure 4h. Obviously, distinct fast charge transfer nanochannels are formed surrounding the oxygen species, beneficial to the rapid transfer of the charge carriers. Hence, these theoretical results indicate that the oxygen passivation can not only optimize the energy band and eliminate the trap states, but also generate charge carries nanochannels for realizing the photocurrent enhancement, agreeing well with the experimental findings.

In conclusion, the horizontally aligned triangular prism cubic $CsPbBr_3$ MW arrays with specific terminated (100) crystal planes were realized on the muscovite mica substrate. Based on these (100) surfaces, photodetectors exhibited excellent optoelectronic performance, including an ultrahigh on/off ratio of up to 5×10^4, a large responsivity of 263 A W^{-1}, a high detectivity of 1.06×10^{12} Jones, and an ultrafast response <100 µs. Significantly, these (100) surfaces exhibited outstanding long-term stability >3000 h in the ambient environment. Photocurrent enhancement and fewer trap states have also been discovered in the (100) surface of perovskite MWs owing to the surface passivation effect of oxygen. The passivation mechanism was further verified through theoretical simulations, providing a guideline to eliminate deep traps and enhance photoconductivity by the specific surface engineering strategy on perovskites.

3 Experimental Section

Synthesis of $CsPbBr_3$ MW Arrays

The $PbBr_2$ (99.999%) and CsBr (99.9%) powders were purchased from Sigma–Aldrich, and no extra purification operation was adopted. First, 100 mg of $PbBr_2$ powders and 70 mg of CsBr powders were fully ground in an agate mortar to form yellow powders. The mixed powders were then pre-annealed at 370°C for 30 min, eventually forming orange powders. Then, a two-zone CVD system was adopted to realize the growth of $CsPbBr_3$ MW arrays. The mixed precursor powders were positioned in the center of 1st heating zone, and the muscovite mica was located downstream (the 2nd heating zone), ≈15 cm away from the source powders. Following, the entire system was evacuated to ≈8 mTorr, and then 150 sccm high-purity Argon gas (Ar, 99.999%) was fed into the tube furnace to act as the carrier gas. The flow rate was then manipulated to 100 sccm, and the growth pressure was regulated to 1.5 Torr. After that, the 1st temperature zone was heated to 480 °C in 50 min and held the temperature for 60 min, while the 2nd temperature zone was held at 330 °C. Eventually, an orange product was grown on the mica with the tube furnace cooling down to room temperature in the Ar atmosphere.

Material Characterizations

The crystalline phases of samples were analyzed through an X-ray diffraction system (D2 Phaser Cu Ka radiation, Bruke). Optical microscope, atomic force microscope (Dimension Icon, Bruker), and scanning electron microscope (quanta 450 FEG, FEI) were adopted to observe the surface morphology of samples. An energy dispersive X-ray (EDX) detector connected with quanta 450 FEG was used to verify the elemental compositions. Nexsa G2 surface analysis system was employed to obtain the X-ray photoelectron spectrometer (XPS) spectrum. The steady-state photoluminescent (PL) spectrum was collected from the F-4600 fluorescence spectrophotometer (HITACHI), while the time-resolved PL results were acquired from HORIBA Fluoromax-4. The in situ PL spectra under different environments were measured in a home-built system based on a spectral CCD array spectrometer (Ocean Optics USB2000), which could be evacuated down to ≈3×10^{-3} Torr and able to inject pure oxygen.

Device Fabrication

A direct evaporation scheme was utilized to fabricate the photodetectors. To fabricate the device, it was began by growing the perovskite MW parallel arrays on a mica substrate. Next, 50 nm thick Au (99.99%) electrodes were thermally evaporated onto the samples, by utilizing a nickel shadow mask with the channel length of 15 µm. This deposition was conducted at a deposition rate of ≈2 Å s^{-1} under high vacuum, where the thickness of the Au electrodes was directly proportional to the deposition time that was monitored by a quartz crystal. Based on the specific terminated crystal planes of the $CsPbBr_3$ MW arrays, the effective area

was calculated considering the two perpendicular (100) and (010) planes. The efficient area (*S*) was calculated as the projection area of these two planes on substrates,

(2)

where *L*, *W*, and *N* represent the channel length, channel width, and the number of MWs, respectively. A standard electrical probe station equipped with the semiconductor analyzer Agilent 4155C was adopted to measure the optoelectronic properties of perovskite MW arrays in the ambient environment, while a high vacuum probe station was used to measure the optoelectronic performance under vacuum. A 450 nm wavelength laser diode was employed to provide the illumination, of which the power density was measured by a PM400 power meter (Thorlabs). The high-precision photoresponse was realized by a high-frequency chopper and recorded by TBS 1102B-EDU digital oscilloscope (Tektronix) connected with a SR570 current preamplifier (Stanford Research Systems).

Acknowledgements

D.L., Y.M., and Y.Z. contributed equally to this work. This work was financially supported by a fellowship award from the Research Grants Council of the Hong Kong Special Administrative Region, China (CityU RFS2021-1S04).

Conflict of Interest

The authors declare no conflict of interest.

Open Research

Data Availability Statement

The data that support the findings of this study are available from the corresponding author upon reasonable request.

Supporting Information

Filename	Description
adfm202302866-sup-0001-SuppMat.pdf 1.8 MB	Supporting Information

References

1 J. Xue, R. Wang, Y. Yang, *Nat. Rev. Mater.* 2020, **5**, 809.

CAS | Web of Science® | Google Scholar

2 a) W. Shockley, *Phys. Rev.* 1939, **56**, 317;

CAS | Web of Science® | Google Scholar

b) S. G. Davison, M. Stęślicka, *Basic Theory of Surface States*, Vol. **46**, Oxford University Press, Oxford, UK 1996.

Google Scholar

3 a) R. Wang, J. Xue, K. L. Wang, Z.-K. Wang, Y. Luo, D. Fenning, G. Xu, S. Nuryyeva, T. Huang, Y. Zhao, *Science* 2019, **366**, 1509;

CAS | PubMed | Web of Science® | Google Scholar

b) H. Min, M. Kim, S. U. Lee, H. Kim, G. Kim, K. Choi, J. H. Lee, S. I. Seok, *Science* 2019, **366**, 749;

CAS | PubMed | Web of Science® | Google Scholar

c) Y.-H. Kim, S. Kim, A. Kakekhani, J. Park, J. Park, Y. H. Lee, H. Xu, S. Nagane, R. B. Wexler, D. H. Kim, *Nat. Photonics* 2021, **15**, 148;

CAS | Web of Science® | Google Scholar

d) Y. Zhao, Y. Qiu, J. Feng, J. Zhao, G. Chen, H. Gao, Y. Zhao, L. Jiang, Y. Wu, *J. Am. Chem. Soc.* 2021, **143**, 8437;

CAS | PubMed | Web of Science® | Google Scholar

e) Y. Zhao, Y. Qiu, H. Gao, J. Feng, G. Chen, L. Jiang, Y. Wu, *Adv. Mater.* 2020, **32**, 1905298.

CAS | Web of Science® | Google Scholar

4 a) J. D. Jackson, *Classical Electrodynamics*, John Wiley & Sons, Hoboken, NJ 2021;

Google Scholar

b) Y. Wang, X. Sun, R. Shivanna, Y. Yang, Z. Chen, Y. Guo, G.-C. Wang, E. Wertz, F. Deschler, Z. Cai, *Nano Lett.* 2016, **16**, 7974.

CAS | PubMed | Web of Science® | Google Scholar

5 S. Dong, Z. Y. Hu, P. Wei, J. Han, Z. Wang, J. Liu, B. L. Su, D. Zhao, Y. Liu, *Adv. Mater.* 2022, **34**, 2204342.

CAS | Web of Science® | Google Scholar

6 a) H. Deng, X. Yang, D. Dong, B. Li, D. Yang, S. Yuan, K. Qiao, Y.-B. Cheng, J. Tang, H. Song, *Nano Lett.* 2015, **15**, 7963;

CAS | PubMed | Web of Science® | Google Scholar

b) I. M. Asuo, D. Gedamu, I. Ka, L. F. Gerlein, F.-X. Fortier, A. Pignolet, S. G. Cloutier, R. Nechache, *Nano Energy* 2018, **51**, 324.

CAS | Web of Science® | Google Scholar

7 H.-H. Fang, S. Adjokatse, H. Wei, J. Yang, G. R. Blake, J. Huang, J. Even, M. A. Loi, *Sci. Adv.* 2016, **2**, e1600534.

PubMed | Web of Science® | Google Scholar

8 a) D. Lu, Y. Zhang, M. Lai, A. Lee, C. Xie, J. Lin, T. Lei, Z. Lin, C. S. Kley, J. Huang, *Nano Lett.* 2018, **18**, 6967;

CAS | PubMed | Web of Science® | Google Scholar

b) Y. Wang, Y. Ren, S. Zhang, J. Wu, J. Song, X. Li, J. Xu, C. H. Sow, H. Zeng, H. Sun, *Commun. Phys.* 2018, **1**, 96.

CAS | Web of Science® | Google Scholar

9 M. Shoaib, X. Zhang, X. Wang, H. Zhou, T. Xu, X. Wang, X. Hu, H. Liu, X. Fan, W. Zheng, *J. Am. Chem. Soc.* 2017, **139**, 15592.

CAS | PubMed | Web of Science® | Google Scholar

10 D. Li, Y. Meng, Y. Zheng, P. Xie, X. Kang, Z. Lai, X. Bu, W. Wang, W. Wang, F. Chen, *Adv. Electron. Mater.* 2022, **8**, 2200727.

CAS | Web of Science® | Google Scholar

11 Y. Fu, M. Yuan, Y. Zhao, M. Dong, Y. Guo, K. Wang, C. Jin, J. Feng, Y. Wu, L. Jiang, *Adv. Funct. Mater.* 2023, **33**, 2214094.

CAS | Web of Science® | Google Scholar

12 J. Chen, Y. Fu, L. Samad, L. Dang, Y. Zhao, S. Shen, L. Guo, S. Jin, *Nano Lett.* 2017, **17**, 460.

CAS | PubMed | Web of Science® | Google Scholar

13 a) X. Mo, X. Li, G. Dai, P. He, J. Sun, H. Huang, J. Yang, *Nanoscale* 2019, **11**, 21386;

CAS | PubMed | Web of Science® | Google Scholar

b) C. Fan, K. Bi, Z. Shu, X. Xu, B. Dai, S. Wang, Z. Qi, J. Wei, H. Duan, Q. Zhang, *J. Phys. D: Appl. Phys.* 2020, **53**, 235105.

CAS | Web of Science® | Google Scholar

14 W. Wang, Y. Meng, W. Wang, Z. Zhang, P. Xie, Z. Lai, X. Bu, Y. Li, C. Liu, Z. Yang, *Adv. Funct. Mater.* 2022, **32**, 2203003.

CAS | Web of Science® | Google Scholar

15 J.-H. Kim, M. R. Bergren, J. C. Park, S. Adhikari, M. Lorke, T. Frauenheim, D.-H. Choe, B. Kim, H. Choi, T. Gregorkiewicz, *Nat. Commun.* 2019, **10**, 5488.

PubMed | Web of Science® | Google Scholar

16 O. Lopez-Sanchez, D. Lembke, M. Kayci, A. Radenovic, A. Kis, *Nat. Nanotechnol.* 2013, **8**, 497.

CAS | PubMed | Web of Science® | Google Scholar

17 D. N. Dirin, I. Cherniukh, S. Yakunin, Y. Shynkarenko, M. V. Kovalenko, *Chem. Mater.* 2016, **28**, 8470.

CAS | PubMed | Web of Science® | Google Scholar

18 a) C. Lan, R. Dong, Z. Zhou, L. Shu, D. Li, S. Yip, J. C. Ho, *Adv. Mater.* 2017, **29**, 1702759;

CAS | Web of Science® | Google Scholar

b) Y. Lee, D. Yoon, S. Yu, H. Sim, Y. Park, Y. S. Nam, K. J. Kim, S. Y. Choi, Y. Kang, J. Son, *Adv. Mater.* 2022, **34**, 2107650.

CAS | Web of Science® | Google Scholar

19 a) S.-C. Liu, Z. Li, Y. Yang, X. Wang, Y.-X. Chen, D.-J. Xue, J.-S. Hu, *J. Am. Chem. Soc.* 2019, **141**, 18075;

CAS | PubMed | Web of Science® | Google Scholar

b) W. Fan, Y. Shi, T. Shi, S. Chu, W. Chen, K. O. Ighodalo, J. Zhao, X. Li, Z. Xiao, *ACS Energy Lett.* 2019, **4**, 2052.

CAS | Web of Science® | Google Scholar

20 a) Y. Wang, Z. Lv, J. Chen, Z. Wang, Y. Zhou, L. Zhou, X. Chen, S. T. Han, *Adv. Mater.* 2018, **30**, 1802883;

PubMed | Web of Science® | Google Scholar

b) Z. Lv, M. Chen, F. Qian, V. A. Roy, W. Ye, D. She, Y. Wang, Z. X. Xu, Y. Zhou, S. T. Han, *Adv. Funct. Mater.* 2019, **29**, 1902374.

Web of Science® | Google Scholar

21 a) M. Lorenzon, L. Sortino, Q. Akkerman, S. Accornero, J. Pedrini, M. Prato, V. Pinchetti, F. Meinardi, L. Manna, S. Brovelli, *Nano Lett.* 2017, **17**, 3844;

CAS | PubMed | Web of Science® | Google Scholar

b) X. Zhu, M. Du, J. Feng, H. Wang, Z. Xu, L. Wang, S. Zuo, C. Wang, Z. Wang, C. Zhang, *Angew. Chem., Int. Ed.* 2021, **60**, 4238;

CAS | PubMed | Web of Science® | Google Scholar

c) X. Zheng, B. Chen, J. Dai, Y. Fang, Y. Bai, Y. Lin, H. Wei, X. C. Zeng, J. Huang, *Nat. Energy* 2017, **2**, 17102.

CAS | Web of Science® | Google Scholar

22 Q. Dong, Y. Fang, Y. Shao, P. Mulligan, J. Qiu, L. Cao, J. Huang, *Science* 2015, **347**, 967.

CAS | PubMed | Web of Science® | Google Scholar

23 a) R. Brenes, C. Eames, V. Bulović, M. S. Islam, S. D. Stranks, *Adv. Mater.* 2018, **30**, 1706208;

PubMed | Web of Science® | Google Scholar

b) Y. Jiang, X. Wang, A. Pan, *Adv. Mater.* 2019, **31**, 1806671.

CAS | PubMed | Web of Science® | Google Scholar

Citing Literature

Download PDF